



# Elementary reaction modeling of CO<sub>2</sub>/H<sub>2</sub>O co-electrolysis cell considering effects of cathode thickness



Wenying Li, Yixiang Shi\*, Yu Luo, Ningsheng Cai

Key Laboratory for Thermal Science and Power Engineering of Ministry of Education, Tsinghua University, Beijing 100084, China

## HIGHLIGHTS

- Elementary reaction modeling for solid oxide CO<sub>2</sub>/H<sub>2</sub>O co-electrolysis cell.
- Effects of cathode thickness on co-electrolysis performance.
- Heterogeneous reaction/electrochemical reaction zones.

## ARTICLE INFO

### Article history:

Received 8 February 2013

Received in revised form

21 May 2013

Accepted 23 May 2013

Available online 6 June 2013

### Keywords:

Solid oxide electrolysis cell  
Carbon dioxide/steam co-electrolysis  
Elementary reaction model  
Cathode thickness  
Heterogeneous chemistry  
Electrochemistry

## ABSTRACT

A one-dimensional elementary reaction model of CO<sub>2</sub>/H<sub>2</sub>O co-electrolysis in solid oxide electrolysis cell (SOEC) coupled with heterogeneous elementary reactions, electrochemical reactions, electrode micro-structure, and the transport of mass and charge is developed in this paper. This model, validated with the experimental performance of H<sub>2</sub>O electrolysis, CO<sub>2</sub> electrolysis and CO<sub>2</sub>/H<sub>2</sub>O co-electrolysis at 700 °C, is demonstrated to be a useful tool for understanding the intricate reaction and transport processes within SOEC electrode and the electrode structure design and optimization. The simulation results indicate that the heterogeneous reactions reach the equilibrium near the cathode outside surface, and the electrochemical reactions mainly occur in the electrode near the electrode–electrolyte interface. The main zone of electrochemical reactions is far enough from the main zone of heterogeneous reactions, so that the two kinds of reactions almost don't influence each other when the cathode is thick enough (e.g. 700 μm). While, as the cathode thickness reduces, the zones of electrochemical reactions and the non-equilibrium heterogeneous reactions overlap each other, and the electrochemical performance of CO<sub>2</sub>/H<sub>2</sub>O co-electrolysis is affected by the variations of elementary species concentrations of O(Ni) and (Ni) due to the heterogeneous reactions. The model successfully explains the experimental phenomenon that the polarization curve of CO<sub>2</sub>/H<sub>2</sub>O electrolysis lies between that of H<sub>2</sub>O and CO<sub>2</sub> electrolysis in a cathode supported SOEC, but almost the same as that of H<sub>2</sub>O electrolysis in an electrolyte supported SOEC.

© 2013 Elsevier B.V. All rights reserved.

## 1. Introduction

Due to the fossil fuel crisis and global warming, increasing interests lay in carbon dioxide capture, utilization and storage. High temperature CO<sub>2</sub>/H<sub>2</sub>O co-electrolysis in solid oxide electrolysis cells (SOECs) was identified as one of the most promising, feasible routes to convert CO<sub>2</sub> and H<sub>2</sub>O to the fuel [1], and as a new energy storage way to transfer the renewable, discontinuous and high on-grid cost electricity generated from solar or wind sources to the fuel which is easier to transport. In SOECs, CO<sub>2</sub> and H<sub>2</sub>O can be converted to syngas (CO + H<sub>2</sub>) and pure oxygen via H<sub>2</sub>O electrolysis, CO<sub>2</sub>

electrolysis and reversible water gas shift (RWGS) reaction [2]. The syngas can be further used as the feedstock for the Fischer–Tropsch (F–T) process to produce hydrocarbon fuel.

Current studies on CO<sub>2</sub>/H<sub>2</sub>O co-electrolysis in SOECs mostly focus on performance testing [3–5], materials development [6] and system analysis and design [7–9]. So far, two experimental SOEC stacks facilities have been respectively demonstrated by Risø National Laboratory (RNL) [10] and Idaho National Laboratory (INL) [11]. INL developed a 15 kW integrated laboratory scale SOEC facility, built a system model of large-scale syngas production powered by nuclear energy, and obtained a highest theoretical overall syngas production efficiency of 48.3% [8]. Subsequently, Becker et al. [9] created a SOEC/F–T system model based on INL's experimental data. The simulation results indicated that the liquid fuels production cost ranges from 4.4 \$ GGE<sup>−1</sup> (Gasoline gallon

\* Corresponding author. Tel./fax: +86 10 62789955.

E-mail address: [shyx@tsinghua.edu.cn](mailto:shyx@tsinghua.edu.cn) (Y. Shi).

equivalent) to 15.0 \$ GGE<sup>-1</sup> for electricity prices of from 0.02 \$ kWh<sup>-1</sup> to 0.14 \$ kWh<sup>-1</sup>. The cost is still quite higher than the cost of crude oil. Therefore, researchers have generally recognized that to accelerate the commercialization process of CO<sub>2</sub>/H<sub>2</sub>O co-electrolysis in SOECs, reducing fabrication cost, developing performance and reliability are the most significant objects, and then to reveal the reaction mechanism governing SOEC performance is the foundation for the CO<sub>2</sub>/H<sub>2</sub>O co-electrolysis research at present.

After introducing CO<sub>2</sub> into H<sub>2</sub>O electrolysis, RWGS reaction occurs in the SOEC cathode and complicates the reaction mechanism. Many studies focused on the influence of RWGS reaction by comparing the electrochemical performance of CO<sub>2</sub>/H<sub>2</sub>O co-electrolysis, H<sub>2</sub>O and CO<sub>2</sub> electrolysis. However, they obtained some inconsistent experimental results of CO<sub>2</sub>/H<sub>2</sub>O co-electrolysis performance as shown in Table 1 concluded from several published literatures [3,4,6,12]. The four series of experiments utilized the same cathode material Ni–YSZ and similar gas composition, but performed two different results. The results of INL [3] and Korea Advanced Institute of Science and Technology [6] both represented that the polarization curves and area specific resistance (ASR) of CO<sub>2</sub>/H<sub>2</sub>O co-electrolysis were almost the same as that of H<sub>2</sub>O electrolysis. They speculated that only H<sub>2</sub>O not CO<sub>2</sub> participated in the cathode electrochemical reduction and the product CO was all generated from the RWGS reaction. Meanwhile, the results of RNL [4] and our previous work [12] both showed that the polarization curves and electrochemical impedance spectrum (EIS) of CO<sub>2</sub>/H<sub>2</sub>O co-electrolysis lied between those of H<sub>2</sub>O and CO<sub>2</sub> electrolysis. They suggested both H<sub>2</sub>O and CO<sub>2</sub> are electrolyzed in the porous cathode and CO was partial generated from the RWGS reaction. Ebbesen et al. [13] in RNL have discovered the inconsistency and suggested that the different gas compositions, namely different conversion resistances contributed to the different results. Nonetheless, Kim-Lohsoontorn et al. [6] applied the same reactant/product molar ratio of 1 as RNL and then obtained the different conclusion. Comparing the experimental conditions listed in Table 1, we proposed that the supported types or cathode thickness of the SOECs could be one of the important reasons for the experimental phenomenon.

Intricate electrochemical reactions, heterogeneous catalysis, mass and charge transfer, flow and heat transfer process exist in a running SOEC. Since the experimental tool is limited to clarify the physical phenomenon, a validated mechanistic model can be a complementary tool to help understand the complex reaction and transport processes.

Several SOEC models of H<sub>2</sub>O electrolysis [14–17] and CO<sub>2</sub> electrolysis [18–20] have been developed to study reactions and transport phenomena in the electrode, but few studies have focused on modeling CO<sub>2</sub>/H<sub>2</sub>O co-electrolysis. Ni [21,22] developed

a one-dimensional and a two-dimensional thermal-fluid model of CO<sub>2</sub>/H<sub>2</sub>O co-electrolysis to study the distribution of gas composition and the behavior of reversible RWGS and methanation reactions in the cathode. Recently, the elementary reaction models have been applied in SOFCs [23–26] to describe the detailed adsorption/desorption and surface reactions on the catalyst surface. Thus, it is also very important to develop an elementary reaction model of CO<sub>2</sub>/H<sub>2</sub>O co-electrolysis in SOECs to understand the reaction and transport mechanisms, which will be beneficial for the experimental results interpretation, cell design and optimizations.

In this paper, an elementary reaction model of CO<sub>2</sub>/H<sub>2</sub>O co-electrolysis cell coupled with cathode elementary heterogeneous reactions and electrochemical charge transfer reactions was developed. This model was calibrated and validated with the experimental data obtained from a SOEC button cell in H<sub>2</sub>O electrolysis, CO<sub>2</sub> electrolysis and CO<sub>2</sub>/H<sub>2</sub>O co-electrolysis modes at 700 °C. The effects of elementary reactions, operating voltage and cathode thickness were discussed. Finally, the different experimental phenomenon can be successfully predicted by this elementary reaction model through changing the cathode thickness.

## 2. Model development

### 2.1. Model assumptions and geometry

The model assumptions are shown as follows:

- (1) All gases are assumed to be ideal gases.
- (2) The cell temperature is uniformly distributed. All parameters are evaluated at the given temperature.
- (3) The convection diffusion caused by pressure gradient in the porous electrodes is ignored.
- (4) The heterogeneous chemical and electrochemical reactions in the cathode are assumed to occur on the Ni surface and at the triple phase boundary (TPB), respectively.
- (5) For simplicity, it is assumed that the distributions of electronic and ionic conductors in electrodes are uniform and continuous, and the electrodes are isotropic media with stable and porous microstructures.
- (6) The effect of carbon deposition on the electrodes is neglected.
- (7) The charge transfer reactions are assumed to take place in only one step.
- (8) The mean field approximation is applied in cathode heterogeneous reactions to assume that the surface adsorbates are uniformly distributed on the surface of Ni catalysts.
- (9) The microscale transfer of surface species caused by surface diffusion is ignored.

**Table 1**

Different experimental results of CO<sub>2</sub>/H<sub>2</sub>O co-electrolysis performance in SOECs concluded from published literatures.

Research institute	Material	Cell type	Cathode gas composition	Experimental result
Idaho National Laboratory [3]	Ni–YSZ YSZ LSM	Cell stacks, electrolyte supported	54.8/22.5/22.7 H <sub>2</sub> O/H <sub>2</sub> /N <sub>2</sub> 100 CO <sub>2</sub> 54.9/22.5/22.6 H <sub>2</sub> O/H <sub>2</sub> /CO <sub>2</sub>	The electrochemical performance for CO <sub>2</sub> /H <sub>2</sub> O co-electrolysis is almost the same as that for H <sub>2</sub> O electrolysis.
Korea Advanced Institute of Science and Technology [6]	Ni–YSZ YSZ Pt	Button cell, electrolyte supported	38/38/24 H <sub>2</sub> O/H <sub>2</sub> /N <sub>2</sub> 25/25/50 CO <sub>2</sub> /CO/N <sub>2</sub> 22/22/22/22/12 CO <sub>2</sub> /CO/H <sub>2</sub> O/H <sub>2</sub> /N <sub>2</sub>	
Risø National Laboratory [4]	Ni–YSZ YSZ LSM–YSZ	Planar cell, cathode supported	50/50 H <sub>2</sub> O/H <sub>2</sub> 50/50 CO <sub>2</sub> /CO 25/25/25/25 CO <sub>2</sub> /CO/H <sub>2</sub> O/H <sub>2</sub>	The electrochemical performance for CO <sub>2</sub> /H <sub>2</sub> O co-electrolysis lies between that for H <sub>2</sub> O and CO <sub>2</sub> electrolysis
Tsinghua University [12]	Ni–YSZ ScSZ LSM–ScSZ	Button cell, cathode supported	28.6/14.3/57.1 H <sub>2</sub> O/H <sub>2</sub> /Ar 28.6/14.3/57.1 CO <sub>2</sub> /CO/Ar 28.6/28.6/14.3/28.5 CO <sub>2</sub> /H <sub>2</sub> O/H <sub>2</sub> /Ar	

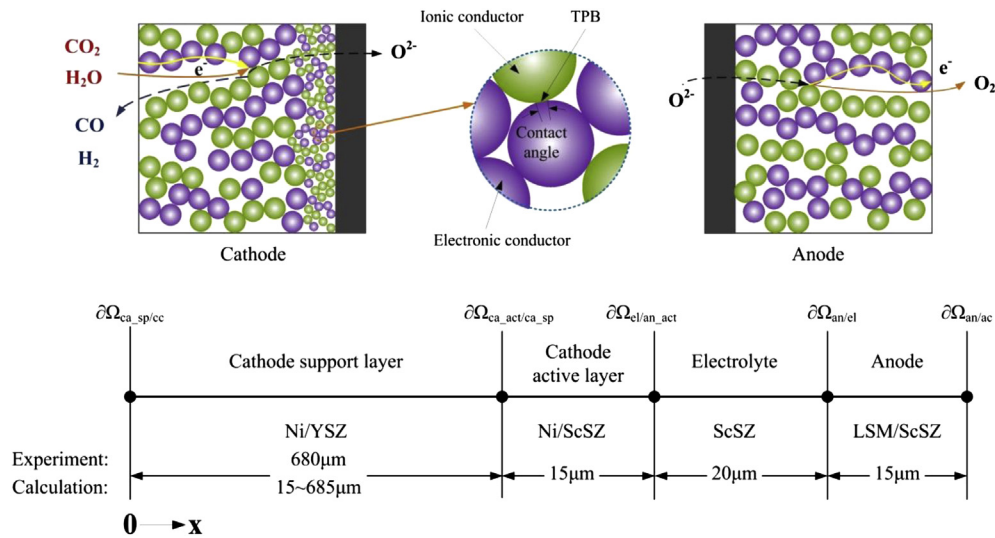


Fig. 1. Model structures, calculation domains and boundaries of CO<sub>2</sub>/H<sub>2</sub>O co-electrolysis.

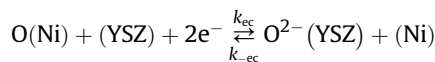
To decrease the computational complexity, we only care about parameters distribution in the cathode thickness direction, and neglect the non-uniformity in the radial direction. A one-dimensional geometry is adopted in this simulation, as shown in Fig. 1 with the model structures, calculation domains and boundaries. With the above assumptions and simplified model geometry, a one-dimensional SOEC model is built coupled with cathode heterogeneous chemistry, electrochemistry, charge balance and mass balance.

## 2.2. Cathode heterogeneous reaction mechanism and electrochemical reaction

Within the cathode, the pore size is comparable to the molecular mean-free-path length and there is very little chance for gas–gas collisions [23]. Thus, the gas-phase reactions are neglected and only

the heterogeneous reactions and electrochemical reaction is considered in the cathode. A heterogeneous reaction mechanism on Ni-based catalysts at temperature of 220–1700 °C is given in Table 2, simplified from the works of Hecht et al. [23] and Janardhanan et al. [27] 18 irreversible reactions, 5 gas species and 7 surface-adsorbed species on Ni catalyst are considered in the simplified mechanism.

In order to keep the consistency of electrochemical and heterogeneous reactions, a one-step interface electrochemical reaction is used in the simulation [28]:



where  $k_{ec}$  and  $k_{-ec}$  are the forward and reverse electrochemical reaction rates, respectively.

Table 2  
Heterogeneous reaction mechanism on Ni-based catalysts.

	Reaction	$A$ (cm, mol, s) <sup>a</sup>	$n^a$	$E$ (kJ mol <sup>-1</sup> ) <sup>a</sup>
<i>Adsorption and desorption</i>				
1 <sup>f</sup>	$\text{H}_2(\text{g}) + (\text{Ni}) \rightarrow \text{H}(\text{Ni}) + \text{H}(\text{Ni})$	$1.000 \times 10^{-02b}$	0.0	0.00
1 <sup>r</sup>	$\text{H}(\text{Ni}) + \text{H}(\text{Ni}) \rightarrow (\text{Ni}) + (\text{Ni}) + \text{H}_2(\text{g})$	$2.545 \times 10^{+19}$	0.0	81.21
2 <sup>f</sup>	$\text{O}_2(\text{g}) + (\text{Ni}) \rightarrow \text{O}(\text{Ni}) + \text{O}(\text{Ni})$	$1.000 \times 10^{-02b}$	0.0	0.00
2 <sup>r</sup>	$\text{O}(\text{Ni}) + \text{O}(\text{Ni}) \rightarrow (\text{Ni}) + (\text{Ni}) + \text{O}_2(\text{g})$	$4.283 \times 10^{+23}$	0.0	474.95
3 <sup>f</sup>	$\text{H}_2\text{O}(\text{g}) + (\text{Ni}) \rightarrow \text{H}_2\text{O}(\text{Ni})$	$0.100 \times 10^{-00b}$	0.0	0.00
3 <sup>r</sup>	$\text{H}_2\text{O}(\text{Ni}) \rightarrow (\text{Ni}) + \text{H}_2\text{O}(\text{g})$	$3.732 \times 10^{+12}$	0.0	60.79
4 <sup>f</sup>	$\text{CO}_2(\text{g}) + (\text{Ni}) \rightarrow \text{CO}_2(\text{Ni})$	$1.000 \times 10^{-05b}$	0.0	0.00
4 <sup>r</sup>	$\text{CO}_2(\text{Ni}) \rightarrow (\text{Ni}) + \text{CO}_2(\text{g})$	$6.447 \times 10^{+07}$	0.0	25.98
5 <sup>f</sup>	$\text{CO}(\text{g}) + (\text{Ni}) \rightarrow \text{CO}(\text{Ni})$	$5.000 \times 10^{-02b}$	0.0	0.00
5 <sup>r</sup>	$\text{CO}(\text{Ni}) \rightarrow (\text{Ni}) + \text{CO}(\text{g})$	$3.563 \times 10^{+11}$	0.0	111.27
	$\theta_{\text{CO}(\text{s})}$			-50.00 <sup>c</sup>
<i>Surface reactions</i>				
6 <sup>f</sup>	$\text{H}(\text{Ni}) + \text{O}(\text{Ni}) \rightarrow \text{OH}(\text{Ni}) + (\text{Ni})$	$5.000 \times 10^{+22}$	0.0	97.90
6 <sup>r</sup>	$\text{OH}(\text{Ni}) + (\text{Ni}) \rightarrow \text{H}(\text{Ni}) + \text{O}(\text{Ni})$	$1.781 \times 10^{+21}$	0.0	36.09
7 <sup>f</sup>	$\text{H}(\text{Ni}) + \text{OH}(\text{Ni}) \rightarrow \text{H}_2\text{O}(\text{Ni}) + (\text{Ni})$	$3.000 \times 10^{+20}$	0.0	42.70
7 <sup>r</sup>	$\text{H}_2\text{O}(\text{Ni}) + (\text{Ni}) \rightarrow \text{H}(\text{Ni}) + \text{OH}(\text{Ni})$	$2.271 \times 10^{+21}$	0.0	91.76
8 <sup>f</sup>	$\text{OH}(\text{Ni}) + \text{OH}(\text{Ni}) \rightarrow \text{H}_2\text{O}(\text{Ni}) + \text{O}(\text{Ni})$	$3.000 \times 10^{+21}$	0.0	100.00
8 <sup>r</sup>	$\text{H}_2\text{O}(\text{Ni}) + \text{O}(\text{Ni}) \rightarrow \text{OH}(\text{Ni}) + \text{OH}(\text{Ni})$	$6.373 \times 10^{+23}$	0.0	210.86
9 <sup>f</sup>	$\text{CO}(\text{Ni}) + \text{O}(\text{Ni}) \rightarrow \text{CO}_2(\text{Ni}) + (\text{Ni})$	$2.000 \times 10^{+19}$	0.0	123.60
	$\theta_{\text{CO}(\text{s})}$			-50.00 <sup>c</sup>
9 <sup>r</sup>	$\text{CO}_2(\text{Ni}) + (\text{Ni}) \rightarrow \text{CO}(\text{Ni}) + \text{O}(\text{Ni})$	$4.653 \times 10^{+23}$	-1.0	89.32

<sup>a</sup> Arrhenius parameters for the rate constant written in the form:  $k = AT^n \exp(-E/RT)$ .

<sup>b</sup> Sticking coefficient.

<sup>c</sup> Coverage dependent activation energy.

(Ni) denotes the free surface active sites on the Ni surface and (YSZ) denotes the oxygen vacancy in the YSZ ionic conductor.

### 2.3. Governing equations

The governing equations for cathode heterogeneous chemistry, cathode electrochemistry, charge and mass balance are summarized in Table 3, which are described in details in our previous work [29–33]. The calculation of the TPB active area per unit volume  $S_{TPB}$  and the effective Ni surface area per unit volume  $S_{Ni}$  is based on the particle coordination number theory in binary random packing of spheres and the percolation theory [34,35]. The extended Fick's model (EFM) considering Knudsen diffusion and molecular diffusion [35–38] is used to describe the mass transfer in the porous electrodes and the effect of finite pressure gradient is neglected.

**Table 3**  
Governing equations for the model.

<i>Cathode heterogeneous chemistry</i>	
General form of adsorption-desorption reactions and surface reactions	$\sum_{k=1}^{K_s+K_i} \nu'_k \chi_k \rightleftharpoons \sum_{k=1}^{K_s+K_i} \nu''_k \chi_k$
The net molar production rate of gaseous or surface components in a heterogeneous reaction	$\dot{s}_k = \sum_{i=1}^N (\nu''_{ki} - \nu'_{ki}) k_i \prod_{k=1}^{K_s+K_i} c_k^{\nu'_{ki}}$
The reaction rate constant for the surface reactions and desorption reactions in the Arrhenius form [27]	$k_i = A_i T^{\eta_i} \exp\left(-\frac{E_i}{RT}\right) \prod_{k=1}^{K_s+K_i} \theta_k^{\mu_{ki}} \exp\left(-\frac{\varepsilon_{ki} \theta_k}{RT}\right)$
The reaction rate constant for adsorption reactions[38]	$k_i = \frac{S_0}{\Gamma^{\nu_i}} \sqrt{\frac{RT}{2\pi W}}$
The sticking coefficient	$S_i^0 = a_i T^{b_i} \exp\left(-\frac{d_i}{RT}\right)$
<i>Cathode electrochemistry</i>	
The current source in the cathode	$Q_{ca} = 2F(k_{ec} c_{O(Ni)} c_{(YSZ)} - k_{-ec} c_{O^{2-}(YSZ)} c_{(Ni)}) S_{TPB}$
The forward electrochemical reaction rates [28]	$k_{ec} = \frac{i_0}{FS_{TPB} c_{O(Ni)}^0 c_{(YSZ)}^0} \exp\left[-2(1-\alpha) \frac{F\eta_{ca}}{RT}\right]$
The reverse electrochemical reaction rates [28]	$k_{-ec} = \frac{i_0}{FS_{TPB} c_{O^{2-}(YSZ)}^0 c_{(Ni)}^0} \exp\left(-2\alpha \frac{F\eta_{ca}}{RT}\right)$
The cathode overpotential	$\eta_{ca} = V_{elec,ca} - V_{ion,ca} - V_{ref,ca}$
The TPB active area per unit volume [34,35]	$S_{TPB} = \frac{\pi \sin^2 \theta_{ep} n_t n_{ep} Z_{ep} Z_{ep} P_{ep} P_p}{Z}$
The effective Ni surface area per unit volume	$S_{Ni} = \pi r_{ep}^2 n_t n_{ep} \left(4 - \frac{\sin^2 \theta_{np} Z_{ep} Z_{ep}}{Z} - \frac{\sin^2 \theta_{nep} Z_{ep} Z_{ep}}{Z}\right)$
<i>Charge balance</i>	
The ionic charge equation in cathode	$\nabla \cdot (-\sigma_{ion,ca}^{eff} \nabla V_{ion,ca}) = Q_{ion,ca}$
The electronic charge equation in cathode	$\nabla \cdot (-\sigma_{elec,ca}^{eff} \nabla V_{elec,ca}) = Q_{elec,ca} = -Q_{ion,ca}$
The ionic charge equation in anode[34]	$\nabla \cdot (-\sigma_{ion,an}^{eff} \nabla V_{ion,an}) = Q_{ion,an}$
The electronic charge equation in anode	$= -i_{0,an} S_{TPB,an} \left\{ \frac{c_{O_2}^{TPB}}{c_{O_2}^{bulk}} \exp\left(\frac{2\alpha F \eta_{an}}{RT}\right) - \exp\left[-\frac{2(1-\alpha) F \eta_{an}}{RT}\right] \right\}$
The ionic charge equation in electrolyte	$\nabla \cdot (-\sigma_{elec,an}^{eff} \nabla V_{elec,an}) = Q_{elec,an} = -Q_{ion,an}$
The anode overpotential	$\nabla \cdot (-\sigma_{ion,el}^{eff} \nabla V_{ion,el}) = 0$
The anode exchange current density [32]	$\eta_{an} = V_{elec,an} - V_{ion,an} - V_{ref,an}$
<i>Mass balance</i>	$i_{0,an} = \frac{\beta RT}{4F} \exp\left(-\frac{E_{an}}{RT}\right) (p_{O_2})^{0.25}$
The mass balance equation in porous electrode	$\nabla \cdot (-D_k^{eff} \nabla c_{k,g}) = R_{k,g}$
The effective diffusivity of gas species $k$ [35]	$D_k^{eff} = \left( \frac{1}{D_{k,mole}^{eff}} + \frac{1}{D_{k,Kn}^{eff}} \right)^{-1}$
The effective molecular diffusion coefficient [38]	$D_{k,mole}^{eff} = \left[ \frac{1-x_k}{\sum_{j \neq k}^n (x_j / D_{kj}^{eff})} \right]$
The effective binary molecular diffusion coefficient [35–37]	$D_{k,j}^{eff} = \frac{\varepsilon}{\tau} D_{k,j} = \frac{0.00101 \varepsilon T^{1.75} (1/M_k + 1/M_j)^{1/2}}{\tau p (V_k^{1/3} + V_j^{1/3})^2}$
The effective Knudsen diffusion coefficient [35–37]	$D_{k,Kn}^{eff} = \frac{\varepsilon}{\tau} D_{k,Kn} = \frac{4\sqrt{\pi}}{3\tau} \sqrt{\frac{8RT}{\pi M_k}}$
The source terms of both gas and surface species in cathode	$R_k = S_k^{eff} \cdot \dot{s}_k = S_k^{eff} \cdot \sum_{i=1}^{N+2} (\nu''_{ki} - \nu'_{ki}) k_i \prod_{k=1}^{K_s+K_i+2} c_k^{\nu'_{ki}}$
The source terms in anode	$R_{O_2} = \frac{Q_{elec,an}}{4F}$

### 2.4. Boundary conditions

According to the operation conditions and model simplifications, the boundary conditions of charge and mass balances partial differential equations are listed in Table 4. *Insulation* means the partial derivative is zero, while *continuity* denotes that the flux is continuous of the variables at the boundary.  $c_{g,ca}$  and  $c_{g,an}$  are the molar fractions of gas species in the cathode and anode.  $V_{an}$  is the cell operation voltage in the simulation.

### 2.5. Model parameters

The pore structure parameters are listed in Table 5. The porosity and pore diameter were characterized using mercury porosimeter (Micromeritics AutoPore IV, USA). The mean pore diameter and

**Table 4**  
Boundary conditions.

Boundary	Ionic charge	Electronic charge	Mass balance
$\partial Q_{ca,sp/cc}$	Insulation	Continuity	$C_{g,ca}$
$\partial Q_{ca,act/ca,sp}$	Continuity	Continuity	Continuity
$\partial Q_{el/ca,act}$	Continuity	Insulation	Insulation
$\partial Q_{an/el}$	Continuity	Insulation	Insulation
$\partial Q_{an/ac}$	Insulation	$V_{an}$	$C_{g,an}$

porosity of cathode were found to be 0.599  $\mu\text{m}$  and 0.335. For simplicity, the mean particle diameters of the two conductors are assumed to be the same and equal to the mean pore diameter [39]. An image processing software (ImagJ V1.34) was used to determine the pore size and porosity of each layer compared cathode support layer from SEM image based on quantitative stereology [30]. The results showed that the average pore diameter of the cathode active layer and anode layer is nearly 1.5 and 1.2 times smaller than that of the cathode support layer, but the porosities of all three layers are almost the same. Table 6 lists the value or expression of materials conductivities and other parameters, which is illustrated in details in our previous works [30,33].

## 2.6. Solution method

The calculations of the model were performed using the finite element commercial software COMSOL MULTIPHYSICS® 3.2. The SOEC performance was calculated at a given cell voltage  $V_{an}$  obtained from experiments. The average current density at a given cell voltage was achieved from the local ionic current density in the electrolyte layer. By setting different cell voltages, a complete

**Table 5**  
Pore structure parameters in porous electrode.

Cell layer	Porosity	Mean pore radius ( $\mu\text{m}$ )	$S_{TPB}$ ( $\text{m}^2\text{m}^{-3}$ )	$S_{Ni}$ ( $\text{m}^2\text{m}^{-3}$ )
Cathode support layer	0.335	0.300	$1.43 \times 10^5$	$2.56 \times 10^6$
Cathode active layer	0.335	0.200	$2.14 \times 10^5$	$3.84 \times 10^6$
Anode layer	0.335	0.250	$1.71 \times 10^5$	–

**Table 6**  
Properties and parameters for model calculation.

Property and parameter	Value or expression	Unit
Ionic conductivity ( $\sigma_{ion}$ )		
ScSZ	$6.92 \times 10^4 \cdot \exp(-9681/T)$	$\text{S m}^{-1}$
YSZ	$3.34 \times 10^4 \cdot \exp(-10300/T)$	$\text{S m}^{-1}$
Electronic conductivity ( $\sigma_{elec}$ )		
LSM	$4.2 \times 10^7/T \cdot \exp(-1150/T)$	$\text{S m}^{-1}$
Ni	$3.27 \times 10^6 \cdot (-1065.3/T)$	$\text{S m}^{-1}$
Equivalent ionic conductivity of electrolyte ( $\sigma_{ei}$ )	$(5.32 \times 10^{-3})T - 4.4445^a$	$\text{S m}^{-1}$
Concentration of oxygen interstitial in the YSZ ( $C_{O_2}$ )	$4.45 \times 10^4$	$\text{mol m}^{-2}$
Concentration of oxygen interstitial in the YSZ ( $C_{YSZ}$ )	$4.65 \times 10^3$	$\text{mol m}^{-2}$
Maximum surface sites density ( $\Gamma$ )	$2.6 \times 10^{-5}$	$\text{mol m}^{-2}$

<sup>a</sup> Experimentally measured by EIS.

**Table 7**  
Gas flow rates in the cathode.

Temperature 700 °C	Molar ratio	Gas flow rate ( $\text{mL min}^{-1}$ )				
		H <sub>2</sub> O	H <sub>2</sub>	CO <sub>2</sub>	CO	Ar
CO <sub>2</sub> electrolysis	CO <sub>2</sub> /CO	0.5		25	50	200
		1		50	50	200
		2		100	50	200
H <sub>2</sub> O electrolysis	H <sub>2</sub> O/H <sub>2</sub>	0.5	25	50		200
		1	50	50		200
		2	100	50		200
CO <sub>2</sub> /H <sub>2</sub> O co-electrolysis	CO <sub>2</sub> /H <sub>2</sub> O	1	100	50	100	200

**Table 8**  
Model turning parameters.

Parameter	Value
Cathode tortuosity	2
Anode tortuosity	3
Cathode electrochemical kinetics parameter, $\beta$ ( $\Omega^{-1}\text{m}^{-2}$ )	$5.24 \times 10^{10}$
Cathode charge transfer coefficient, $\alpha_{ca}$	0.35
Anode charge transfer coefficient, $\alpha_{an}$	0.4

polarization curve can be generated. Since some model parameters cannot be determined directly from published literatures, a SOEC experiment is necessary for the model calibration and validation.

## 3. Experiment

### 3.1. SOEC button cell

Cathode supported SOEC button cells made by Shanghai Institute of Ceramics Chinese Academy of Sciences were utilized in this study. The button cell consisted of a Ni–YSZ cathode support layer (680  $\mu\text{m}$ ), a Ni–ScSZ cathode active layer (15  $\mu\text{m}$ ), a ScSZ electrolyte layer (20  $\mu\text{m}$ ) and a LSM–ScSZ anode layer (15  $\mu\text{m}$ ), as shown in Fig. 1. The diameter of anode was 1.3 cm and the diameters of other layers were all 2.6 cm. To collect current from the cell, a reticular layer of silver paste was printed on both surfaces of electrodes by screen-printing.

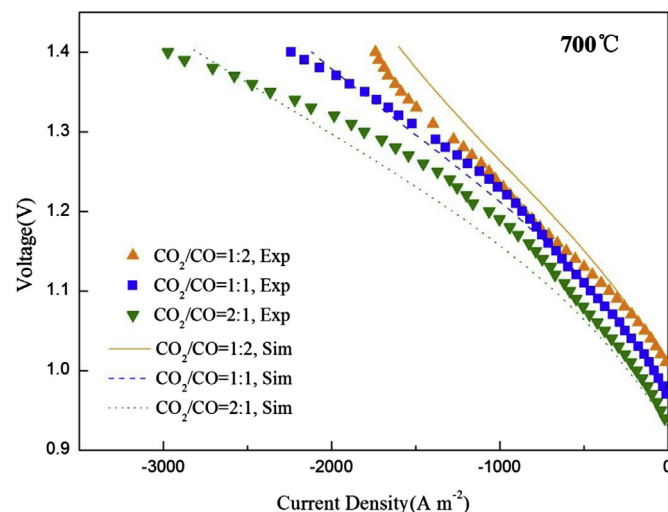


**Fig. 2.** Modeling and experimental polarization curves at 700 °C with CO<sub>2</sub>/CO molar ratio of 0.5, 1 and 2.



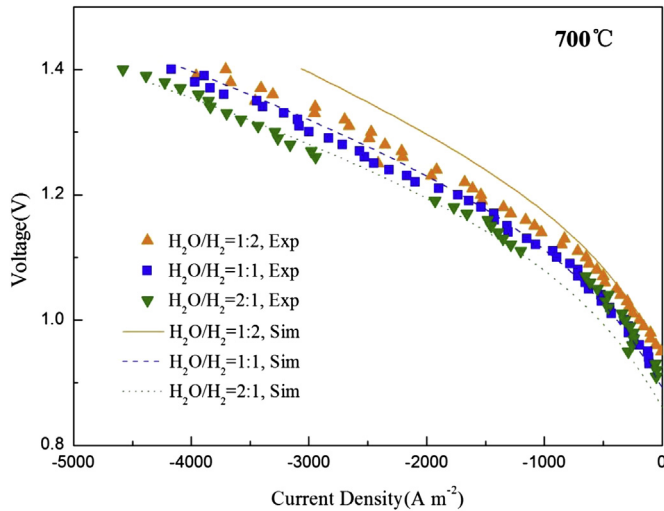


Fig. 3. Modeling and experimental polarization curves at 700 °C with  $\text{H}_2\text{O}/\text{H}_2$  molar ratio of 0.5, 1 and 2.

### 3.2. Testing procedure

A button cell reactor and an experimental measurement system were built for evaluating the cell performance and testing exhaust components, which is described in details in our previous work [33]. The steam was sent into the reactor by the carrier gas Ar through a waterbath. The steam amount and content were adjusted by the carrier gas amount and the temperature of the waterbath. The steam content was tested by a humidity transmitter (Testo6681, Germany) and calibrated by testing the weight increase of calcium chloride anhydrous desiccant within 0.5–2 h.

Before testing, pure  $\text{H}_2$  was sent into the reactor for 1 h at 800 °C to fully reduce the cathode. The operating temperature was stabilized at 700 °C during the whole experiment.  $\text{H}_2\text{O}/\text{H}_2/\text{CO}_2/\text{CO}$  mixtures were used as the cathode gas at given flow rates as shown in Table 7. Ar was used as the cathode carrier gas, while air was supplied to the anode at a steady flow rate of  $150 \text{ mL min}^{-1}$ .

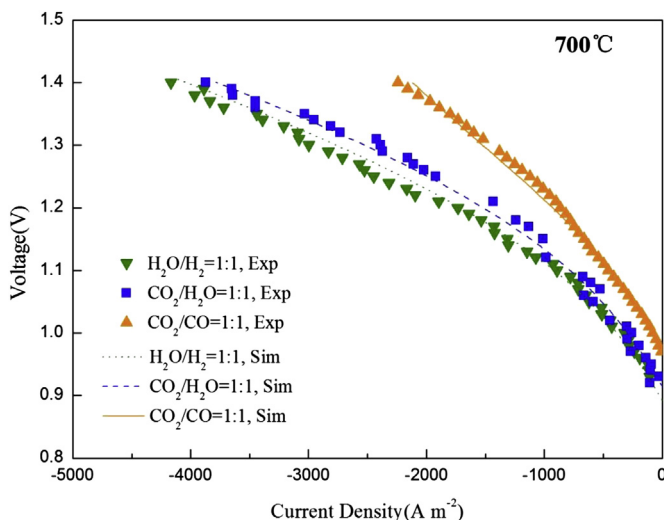


Fig. 4. Modeling and experimental polarization curves of  $\text{H}_2\text{O}$ ,  $\text{CO}_2$  electrolysis and  $\text{CO}_2/\text{H}_2\text{O}$  co-electrolysis at 700 °C.

Table 9

Simulation conditions for  $\text{H}_2\text{O}$ ,  $\text{CO}_2$  electrolysis and  $\text{CO}_2/\text{H}_2\text{O}$  co-electrolysis.

700 °C	Cathode gas composition				Anode gas	Cathode thickness
	$\text{H}_2\text{O}$	$\text{H}_2$	$\text{CO}_2$	CO		
$\text{H}_2\text{O}$ electrolysis	0.5	0.5			Air	30 $\mu\text{m}$ to 700 $\mu\text{m}$ Base case: 700 $\mu\text{m}$
$\text{CO}_2$ electrolysis			0.5	0.5	Air	
$\text{CO}_2/\text{H}_2\text{O}$ co-electrolysis	0.25	0.25	0.25	0.25	Air	

### 4. Model calibration and validation

Since some model parameters are indeterminate, it is imperative to implement the calibration of parameters in a reasonable range to fit the experimental data. These model parameters were tuned based on the experimental polarization curves of the cases with molar ratio of 1 for the three electrolysis modes, as listed in Table 7. The model tuning parameters are summarized in Table 8. Once all the model parameters were determined, they would not be changed in other cases simulations.

Figs. 2 and 3 represent the modeling and experimental polarization curves at 700 °C with  $\text{CO}_2/\text{CO}$  and  $\text{H}_2\text{O}/\text{H}_2$  molar ratio of 0.5, 1 and 2, respectively. It is observed that the modeling results are basically consistent with the experimental results in SOEC mode. When the concentrations of reactants ( $\text{CO}_2$  or  $\text{H}_2\text{O}$ ) increase, the open circuit voltage (OCV) decreases and the cell performance is improved as expected. The modeling results in Fig. 2 agree well with the experimental data at low current density but slightly deviate from experiment at high current density. The simplification of model geometry might be the reason of the non-ignorable derivation. The cathode diameter is larger than the anode diameter, giving rise to a significant non-uniform distribution of gas concentrations in cathode in the radial direction. Thus, the experimental data is not exactly accorded with 1D assumption and the deviation can be more remarkable for the gas with lower diffusion coefficients such as CO and  $\text{CO}_2$  compared to  $\text{H}_2$  and  $\text{H}_2\text{O}$ . Besides, the deviations in Fig. 3 mainly come from the experimental error. In the experiments, the instantaneous amount of steam was not stable and fluctuated in a 2~5% range tested by the humidity transmitter,

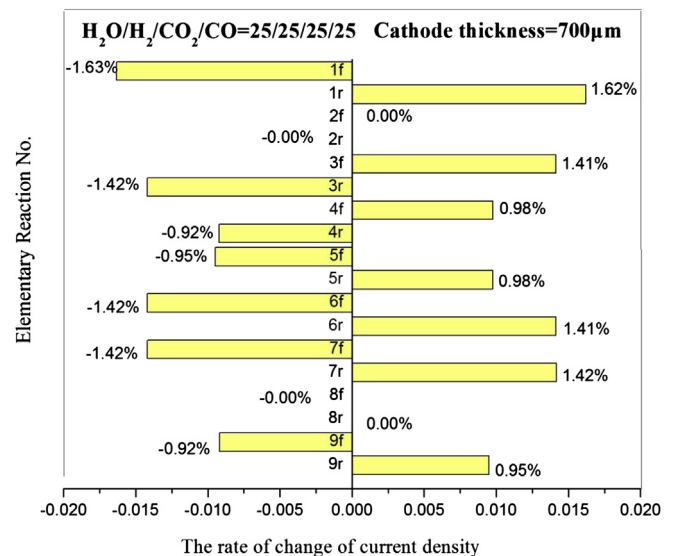


Fig. 5. The rates of change of current density at 1.4 V for  $\text{CO}_2/\text{H}_2\text{O}$  co-electrolysis at 700 °C, when the rate constants of elementary reactions increase by 10%.

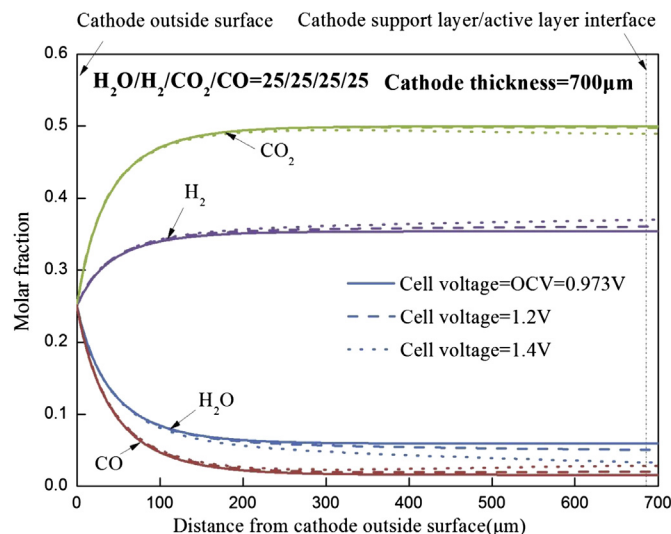


Fig. 6. Molar fractions distributions of  $\text{H}_2\text{O}/\text{H}_2/\text{CO}_2/\text{CO}$  in cathode for  $\text{CO}_2/\text{H}_2\text{O}$  co-electrolysis with different cell operating voltages at  $700^\circ\text{C}$ .

but the error of long-time amount of steam can be ignored according to the long-time weight increase of desiccant.

Fig. 4 shows the modeling and experimental polarization curves for  $\text{H}_2\text{O}$ ,  $\text{CO}_2$  electrolysis and  $\text{CO}_2/\text{H}_2\text{O}$  co-electrolysis at  $700^\circ\text{C}$ . The modeling results for  $\text{CO}_2/\text{H}_2\text{O}$  co-electrolysis accord well with the experimental results. Thereby, it can be convinced that this model is enough accurate to estimate the electrochemical performance of SOECs with  $\text{H}_2\text{O}/\text{H}_2/\text{CO}_2/\text{CO}$  mixtures in cathode at  $700^\circ\text{C}$ .

## 5. Results and discussion

For comparison, the simulation conditions for  $\text{H}_2\text{O}$  electrolysis,  $\text{CO}_2$  electrolysis and  $\text{CO}_2/\text{H}_2\text{O}$  co-electrolysis were all given 50% oxidant and 50% reductant in the cathode, while air was supplied to the anode, as shown in Table 9. The temperature of simulation conditions was kept constant at  $700^\circ\text{C}$ , the same temperature in the experiments.

The OCVs of  $\text{H}_2\text{O}$  electrolysis and  $\text{CO}_2$  electrolysis were formulated by Nernst equations. In general, when  $\text{CO}$  and  $\text{H}_2$  both exist in anode gas in SOFC, it is mostly assumed that  $\text{H}_2$  is the only electrochemically active components, so that the OCV is calculated by the Nernst equation of  $\text{H}_2$  [27]. Thus, the  $\text{CO}_2/\text{H}_2\text{O}$  co-electrolysis

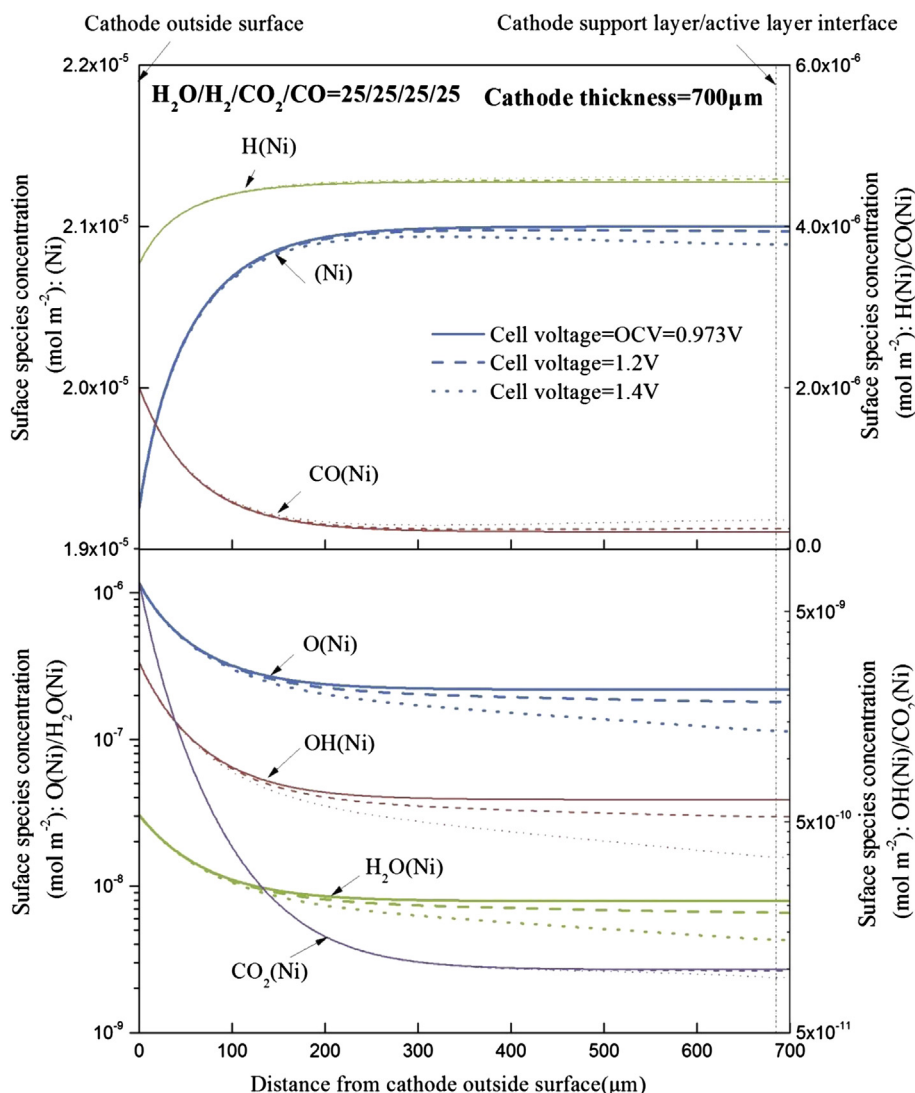
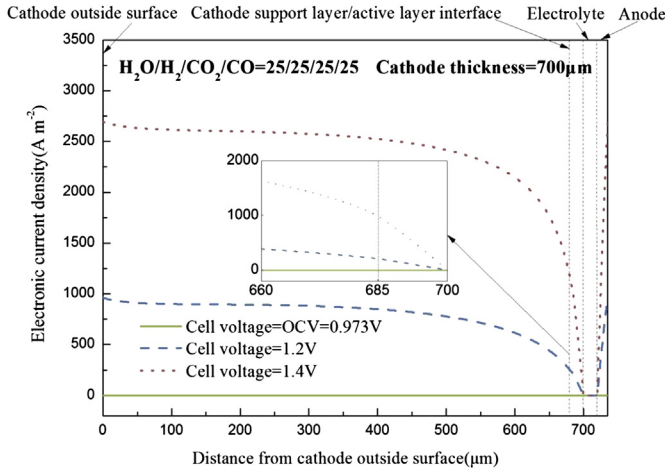


Fig. 7. Surface species concentration distributions of  $\text{CO}_2/\text{H}_2\text{O}$  co-electrolysis in cathode with different cell operating voltages at  $700^\circ\text{C}$ .



**Fig. 8.** Electronic current density distribution of  $\text{CO}_2/\text{H}_2\text{O}$  co-electrolysis with different cell operating voltage at 700 °C in cathode and anode.

was set to the same OCV as  $\text{H}_2\text{O}$  electrolysis here. As one of vital variables in the simulation, the cathode thickness was set in the range of from 30  $\mu\text{m}$  to 700  $\mu\text{m}$  according to the published literatures. For the two layers of the cathode, the thickness of active layer was fixed at 15  $\mu\text{m}$ , while the thickness of support layer changed from 15  $\mu\text{m}$  to 685  $\mu\text{m}$ , as shown in Fig. 1. The cathode thickness of base case was set to 700  $\mu\text{m}$ .

### 5.1. Effects of cathode heterogeneous elementary reactions rate

For more intuitive comparison, the rates of change of current density at 1.4 V for  $\text{CO}_2/\text{H}_2\text{O}$  co-electrolysis at 700 °C when the rate constants  $k$  of the 18 elementary reactions listed in Table 2 increase by 10% are calculated to compare the influence of different elementary reactions on cell performance, as shown in Fig. 5.

From Fig. 5, the relative values of rate of change denote the relative influence degrees of elementary reactions on current density. It is observed that the rates of change of current density for the adsorption/desorption of  $\text{O}_2$  (No. 2<sup>f</sup> and 2<sup>r</sup>) and the reaction of  $\text{OH}(\text{Ni}) + \text{OH}(\text{Ni}) \leftrightarrow \text{H}_2\text{O}(\text{Ni}) + \text{O}(\text{Ni})$  (No. 8<sup>f</sup> and 8<sup>r</sup>) are almost zero. So it can be speculated that the 4 elementary reactions have little impact on the cell performance and almost don't occur in the porous cathode for  $\text{CO}_2/\text{H}_2\text{O}$  co-electrolysis. According to this analysis thought, the order of adsorption/desorption rates for the other 4 gas species in cathode can be directly obtained by the relative values of the rates of change of current density in Fig. 5, which is  $\text{H}_2$  desorption (No. 1<sup>r</sup>) >  $\text{H}_2\text{O}$  adsorption (No. 3<sup>f</sup>) >  $\text{CO}_2$  adsorption (No. 4<sup>f</sup>)  $\approx$   $\text{CO}$  desorption (No. 5<sup>r</sup>). Besides, the main surface reactions include  $\text{H}_2\text{O}(\text{Ni}) + (\text{Ni}) \rightarrow \text{H}(\text{Ni}) + \text{OH}(\text{Ni})$  (No. 7<sup>r</sup>),  $\text{OH}(\text{Ni}) + (\text{Ni}) \rightarrow \text{H}(\text{Ni}) + \text{O}(\text{Ni})$  (No. 6<sup>r</sup>),  $\text{CO}_2(\text{Ni}) + (\text{Ni}) \rightarrow \text{CO}(\text{Ni}) + \text{O}(\text{Ni})$  (No. 9<sup>r</sup>).

It can be further observed that the reaction rates of the whole process of  $\text{CO}_2$  converting to  $\text{CO}$  (No. 4<sup>f</sup> – No. 9<sup>r</sup> – No. 5<sup>r</sup>) are slower than the analogous process of  $\text{H}_2\text{O}$  converting to  $\text{H}_2$  (No. 3<sup>f</sup> – No. 7<sup>r</sup> – No. 6<sup>r</sup> – No. 1<sup>r</sup>). Obviously, for the electrochemical reaction, the amount of  $\text{O}(\text{Ni})$  obtained from  $\text{CO}_2/\text{CO}$  species is smaller than that from  $\text{H}_2\text{O}/\text{H}_2$  species, which signifies that the electrochemical reduction rate of  $\text{H}_2\text{O}$  can be faster than that of  $\text{CO}_2$  during  $\text{CO}_2/\text{H}_2\text{O}$  co-electrolysis process.

### 5.2. Effects of operating voltage

The effects of operating voltage on the molar fraction distributions of gas species in cathode for  $\text{CO}_2/\text{H}_2\text{O}$  co-electrolysis at 700 °C are shown in Fig. 6. The curves at OCV express that the heterogeneous reactions reach the equilibrium within at least 200  $\mu\text{m}$  depth from the cathode outside surface in this simulation. The equilibrium composition is  $\text{H}_2\text{O}/\text{H}_2/\text{CO}_2/\text{CO} = 6/35/49/2$  without external electricity, as the inlet composition is  $\text{H}_2\text{O}/\text{H}_2/\text{CO}_2/\text{CO} = 25/25/25/25$ . Due to the different diffusion coefficients, the variation of  $\text{H}_2\text{O}$  content from initial to equilibrium value is nearly twice than the

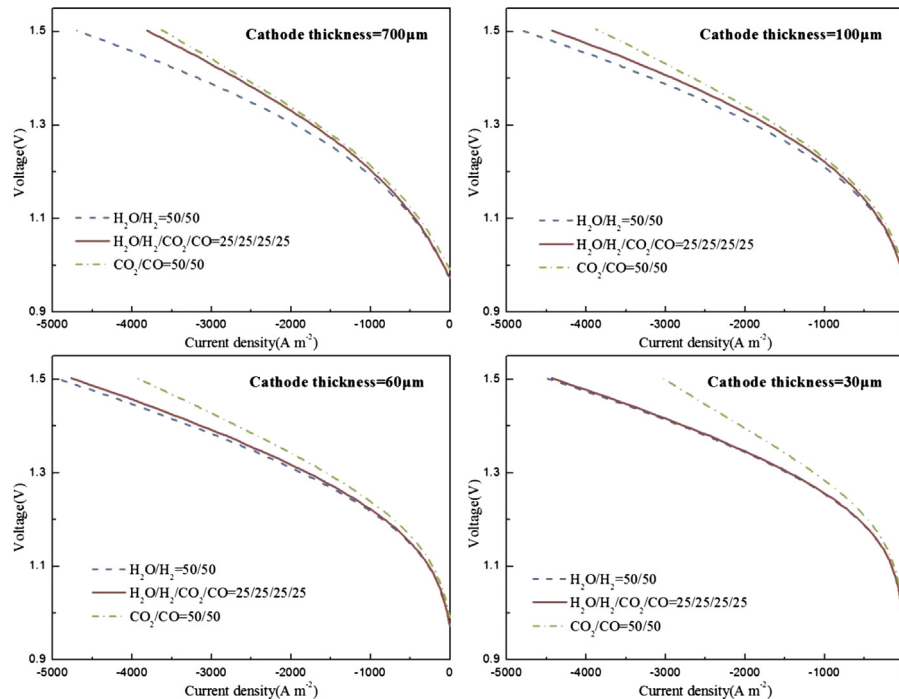


**Fig. 9.** Polarization curves of  $\text{H}_2\text{O}$  electrolysis,  $\text{CO}_2$  electrolysis and  $\text{CO}_2/\text{H}_2\text{O}$  co-electrolysis with different cathode thicknesses (700, 100, 60, 30  $\mu\text{m}$ ) at 700 °C.



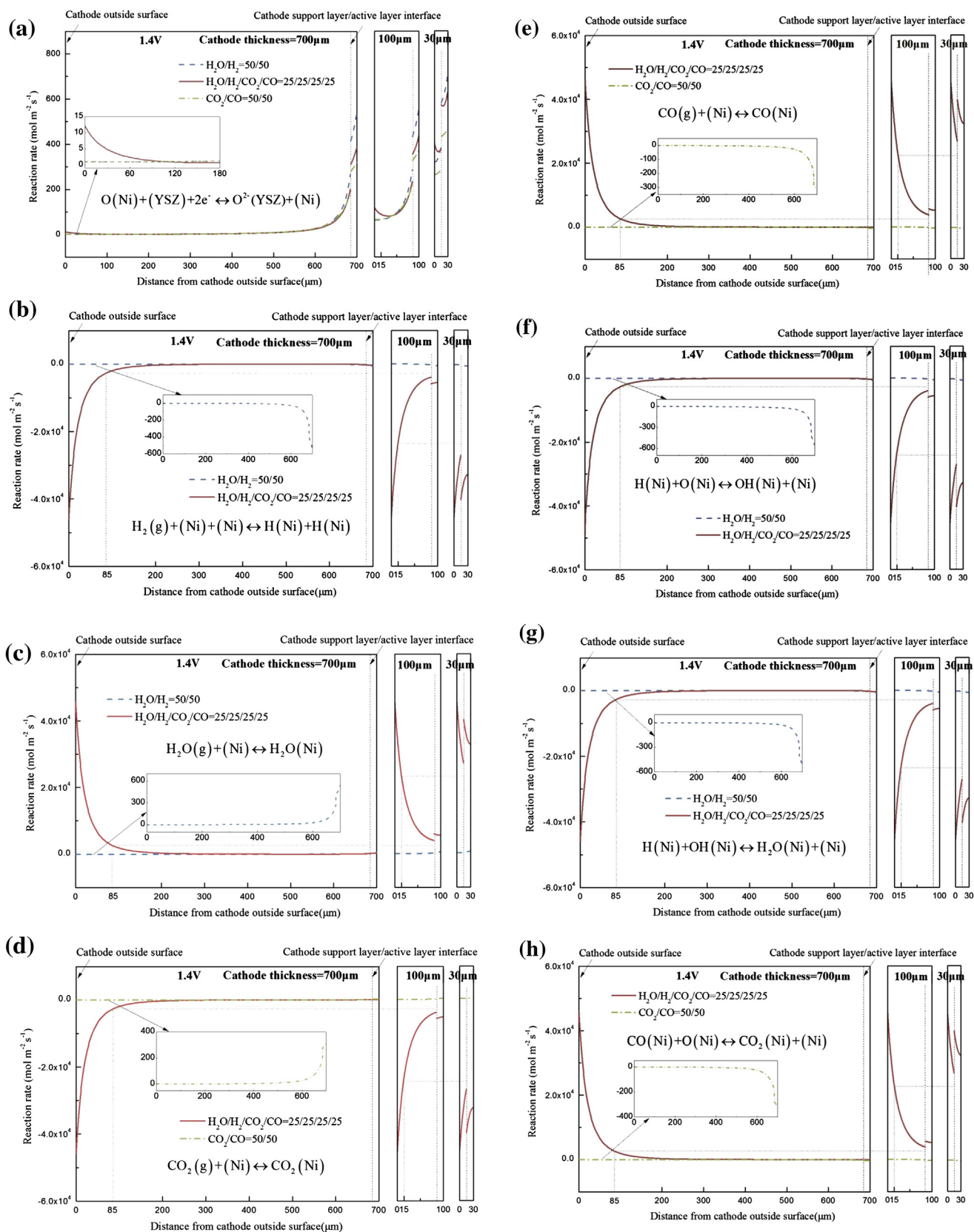


**Fig. 10.** Electrochemical reaction rate (a) and heterogeneous elementary reactions rates (b–h) of H<sub>2</sub>O electrolysis, CO<sub>2</sub> electrolysis and CO<sub>2</sub>/H<sub>2</sub>O co-electrolysis with different cathode thicknesses (700, 100, 30 μm) at 1.4 V.

variation of  $H_2$  content. When applying external voltage, the molar fraction of  $H_2O$  and  $CO_2$  decrease but that of  $H_2$  and  $CO$  increase with operating voltage due to the electrochemical reactions as expected.

Fig. 7 gives the effects of operating voltage on the surface species concentration distribution in cathode for  $CO_2/H_2O$  co-electrolysis at  $700^\circ C$ . (Ni),  $H(Ni)$  and  $CO(Ni)$  are the major surface species on Ni particles in the cathode. The higher voltage contributes to the increasing surface species concentration of  $H(Ni)$  and  $CO(Ni)$  and the decreasing surface species concentration of (Ni),  $O(Ni)$ ,  $OH(Ni)$ ,  $H_2O(Ni)$  and  $CO_2(Ni)$ .

The electronic current density distribution in cathode and anode for  $CO_2/H_2O$  co-electrolysis with different cell operating voltages at  $700^\circ C$  is shown in Fig. 8. It can be observed that the electronic current density significantly increases with the cell voltage. The slope of electronic current density curves represents the degree of electrochemical reactions. The curves in cathode indicate that the electrochemical reactions mainly occur within  $200\ \mu m$  depth from the cathode/electrolyte interface. Due to the higher ionic conductivity and larger TPB active sites per unit volume in the cathode active layer, the reaction rates of electrolysis in the cathode active layer is faster than those in the cathode support layer. The curves in anode shows the electrochemical reactions occur in the whole anode and the slope of electronic current densities or the reaction rates are almost constant. Compared with the distribution in cathode, it is implied that the electrochemical reactions are not fully developed in the thin anode.

### 5.3. Effects of cathode thickness on cell performance

The polarization curves of  $H_2O$  electrolysis,  $CO_2$  electrolysis and  $CO_2/H_2O$  co-electrolysis with different cathode thicknesses at  $700^\circ C$  are shown in Fig. 9. Comparing with the performance of  $H_2O$  and  $CO_2$  electrolysis with the same reactant/product ratio of 1, it can be observed that the cathode thickness significantly affects the relative electrochemical performance of  $CO_2/H_2O$  co-electrolysis. When the cathode thickness equals to  $700\ \mu m$ , the polarization curve of  $CO_2/H_2O$  co-electrolysis lies between that of  $H_2O$  and  $CO_2$  electrolysis, and is closer to  $CO_2$  electrolysis. As the cathode thickness is gradually reduced to  $30\ \mu m$ , the curve of  $CO_2/H_2O$  co-electrolysis gradually approaches to that of  $H_2O$  electrolysis until the two curves coincide with each other. It is indicated that the cell performance of  $CO_2/H_2O$  co-electrolysis can be the same as that of  $H_2O$  electrolysis if the cathode thickness is enough thin. These results are in accord with the different experimental phenomenon listed in Table 1, and explain the main reasons are not only the gas composition or conversion resistance, but also the factors related to the cathode thickness. In addition, when the cathode (or anode) is too thin like  $30\ \mu m$ , the electrochemical reactions cannot fully react in limited TPB active sites, leading to performance degradation. On the other side, the gas and ionic diffusion resistance will also reduce the electrochemical reaction rate when the cathode (or anode) is too thick. So the optimal cathode thickness for  $CO_2/H_2O$  electrolysis is  $60\ \mu m$  in this simulation, and the current density reaches the maximum of  $3135\ A\ m^{-2}$  at  $1.4\ V$  as shown in Fig. 9. The other electrode structure parameters such as porosity, pore diameter and tortuosity can also shift the result, so that the specific optimum thickness of  $60\ \mu m$  is only applied to the simulation conditions here.

In order to figure out what are the main factors caused by the cathode thickness in the heterogeneous chemistry and electrochemistry process, which make the  $CO_2/H_2O$  co-electrolysis performance close to  $H_2O$  electrolysis as the cathode thickness becomes thinner, the electrochemical reaction rate, heterogeneous elementary reaction rates and surface species concentration

distributions effected by the cathode thickness should be studied in details.

The electrochemical reaction rates and main heterogeneous elementary reactions rates of the three electrolysis modes with different cathode thicknesses ( $700, 100, 30\ \mu m$ ) at  $1.4\ V$  are given in Fig. 10. The discontinuity of curves is caused by the different materials characteristics of Ni–YSZ (the cathode support layer) and Ni–ScSZ (the cathode active layer). The rate of electrochemical reaction is 2 orders less than the rate of heterogeneous elementary reactions.

The results in Fig. 10(a) show that the electrochemical reaction rate of  $CO_2/H_2O$  electrolysis are not usually between that of the other two electrolysis modes in the whole porous cathode. The distinction mainly appears in two zones, one is the zone near the cathode outside surface, the other which is more obvious is near the cathode/electrolyte interface. In the first zone, the electrochemical reaction rate of  $CO_2/H_2O$  co-electrolysis is higher than the others and significantly increases with the decreasing of cathode thickness. While, in the last zone, the rate of  $CO_2/H_2O$  co-electrolysis lies between that of  $H_2O$  electrolysis and  $CO_2$  electrolysis and approaches to but not coincide with that of  $H_2O$  electrolysis when the cathode thickness reduces.

According to the electrochemical equation, it can be found the surface species concentrations of  $O(Ni)$  and (Ni) are ones of the major influencing factors which control the reaction rate. Fig. 11 shows the surface species concentration distributions of  $O(Ni)$  and (Ni) in the three electrolysis modes with different cathode thicknesses. The variations of  $O(Ni)$  and (Ni) concentration under  $H_2O$  and  $CO_2$  electrolysis modes are quite smaller than that under  $CO_2/H_2O$  co-electrolysis mode, because the heterogeneous

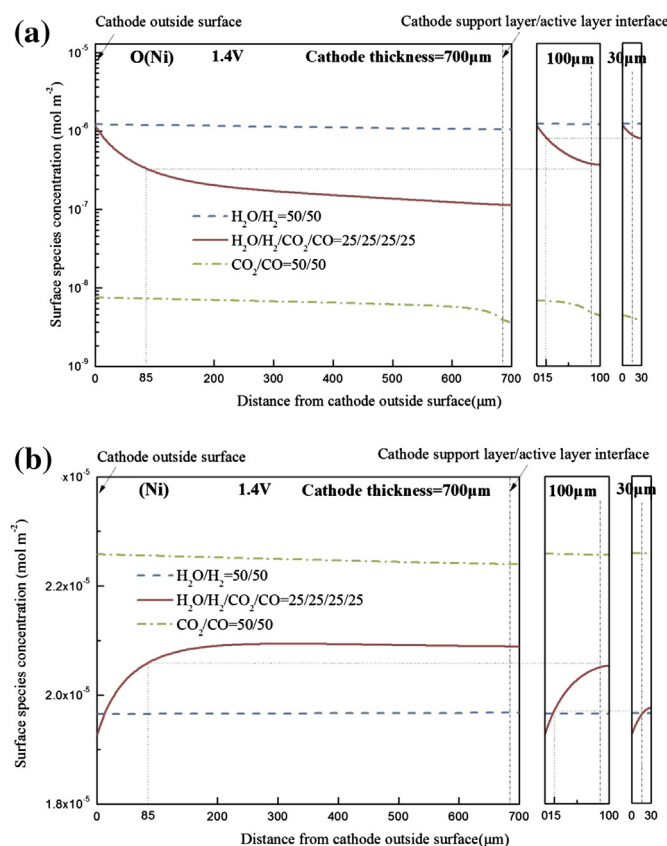


Fig. 11. Surface species concentration distributions of  $O(Ni)$  (a) and (Ni) (b) for  $H_2O$  electrolysis,  $CO_2$  electrolysis and  $CO_2/H_2O$  co-electrolysis with different cathode thickness ( $700, 100, 30\ \mu m$ ) at  $1.4\ V$ .

elementary reactions of  $\text{CO}_2/\text{H}_2\text{O}$  co-electrolysis react 2 orders faster than the other two electrolysis modes, as shown in Fig. 10(b)–(h). As mentioned before, the heterogeneous reactions reach the equilibrium within 200  $\mu\text{m}$  depth from the cathode outside surface, and the electrochemical reactions mainly occur in the electrode near the electrode–electrolyte interface. When the cathode thickness is 700  $\mu\text{m}$ , the main zone of electrochemical reactions is far from that of the heterogeneous reactions, and the electrochemical performance of the SOEC is seldom influenced by the elementary species concentration variations of  $\text{O}(\text{Ni})$  and  $\text{Ni}$  due to the heterogeneous reactions. While, as the cathode thickness reduces, the zones of electrochemical reactions and the non-equilibrium heterogeneous reactions overlap each other, and the average surface species concentration of  $\text{O}(\text{Ni})$  decreases but  $\text{Ni}$  increases, resulting in a higher electrochemical reaction rate of  $\text{CO}_2/\text{H}_2\text{O}$  co-electrolysis. The results can interpret the different experimental phenomenon concluded from several published literatures, which represents that the polarization curve of  $\text{CO}_2/\text{H}_2\text{O}$  electrolysis lies between that of  $\text{H}_2\text{O}$  and  $\text{CO}_2$  electrolysis in a cathode supported SOEC, and almost the same as that of  $\text{H}_2\text{O}$  electrolysis in a electrolyte supported SOEC.

## 6. Conclusion

A detailed one-dimensional elementary reaction model of  $\text{CO}_2/\text{H}_2\text{O}$  co-electrolysis cell was developed by considering the cathode heterogeneous elementary reactions, electrochemical reactions, electrode microstructure and the transport process of mass and charge. The model was validated with the experimental performance for  $\text{H}_2\text{O}$  electrolysis,  $\text{CO}_2$  electrolysis and  $\text{CO}_2/\text{H}_2\text{O}$  co-electrolysis at 700  $^\circ\text{C}$ , and the distributions of species concentrations, reaction rates and current densities were simulated. In this paper, the model is demonstrated to be a useful tool for understanding the intricate reaction and transport processes within SOEC electrode and for the electrode structure design and optimization.

The simulation results of  $\text{CO}_2/\text{H}_2\text{O}$  co-electrolysis indicate that:

- (1) The adsorption/desorption of  $\text{O}_2$  and  $\text{OH}(\text{Ni}) + \text{OH}(\text{Ni}) \leftrightarrow \text{H}_2\text{O}(\text{Ni}) + \text{O}(\text{Ni})$  can hardly react in the porous cathode. The order of adsorption/desorption rates is  $\text{H}_2$  desorption  $>$   $\text{H}_2\text{O}$  adsorption  $>$   $\text{CO}_2$  adsorption  $\approx$   $\text{CO}$  desorption. The main surface reactions include  $\text{H}_2\text{O}(\text{Ni}) + (\text{Ni}) \rightarrow \text{H}(\text{Ni}) + \text{OH}(\text{Ni})$ ,  $\text{OH}(\text{Ni}) + (\text{Ni}) \rightarrow \text{H}(\text{Ni}) + \text{O}(\text{Ni})$  and  $\text{CO}_2(\text{Ni}) + (\text{Ni}) \rightarrow \text{CO}(\text{Ni}) + \text{O}(\text{Ni})$ . The electrochemical reduction rate of  $\text{H}_2\text{O}$  is faster than that of  $\text{CO}_2$ .
- (2)  $\text{Ni}$ ,  $\text{H}(\text{Ni})$  and  $\text{CO}(\text{Ni})$  are the major surface species on the Ni/YSZ cathode surface. As the operating voltage increases, the surface species concentration of  $\text{H}(\text{Ni})$  and  $\text{CO}(\text{Ni})$  increases and the surface species concentration of  $\text{Ni}$ ,  $\text{O}(\text{Ni})$ ,  $\text{OH}(\text{Ni})$ ,  $\text{H}_2\text{O}(\text{Ni})$  and  $\text{CO}_2(\text{Ni})$  decreases.
- (3) The heterogeneous reactions reach the equilibrium within 200  $\mu\text{m}$  depth from the cathode outside surface, and the electrochemical reactions mainly occur in the electrode near the electrode–electrolyte interface. When the cathode is thick enough (e.g. more than 400  $\mu\text{m}$ ), the main zone of electrochemical reactions is far from that of the heterogeneous reactions, and the electrochemical performance of the SOEC is seldom influenced by the elementary species concentration variation due to the heterogeneous reactions. On the other side, as the cathode thickness gradually reduces (e.g. less than 400  $\mu\text{m}$ ), the main zones of electrochemical reactions and the non-equilibrium heterogeneous reactions gradually overlap each other, and the average surface species concentration of  $\text{O}(\text{Ni})$  increases but  $\text{Ni}$  decreases, contributing to a higher average electrochemical reaction rate of  $\text{CO}_2/\text{H}_2\text{O}$  co-electrolysis.

- (4) The polarization curve of  $\text{CO}_2/\text{H}_2\text{O}$  electrolysis lies between that of  $\text{H}_2\text{O}$  and  $\text{CO}_2$  electrolyte with a cathode thickness of 700  $\mu\text{m}$ , and gradually approaches to that of  $\text{H}_2\text{O}$  electrolysis until the two curves coincide with each other as the cathode thickness reduces from 700  $\mu\text{m}$  to 30  $\mu\text{m}$ . The simulation results successfully predict the experimental phenomenon concluded from published literatures.

## Acknowledgments

The study was supported by Projects 51276098 and 51106085 (National Natural Science Foundation of China, NSFC), Doctoral Fund of Ministry of Education of China (No. 20110002120017) and the Ladder Program Project of the Beijing Key Laboratory of  $\text{CO}_2$  Utilization and Reduction Technology (No. Z111109055311094). We also gratefully thank for the offers of button cells used in experiments from Prof. Shaorong Wang in Shanghai Institute of Ceramics Chinese Academy of Sciences.

## Nomenclature

### Abbreviation

ASR	area specific resistance
EIS	electrochemical impedance spectrum
F–T	Fischer–Tropsch
INL	Idaho National Laboratory
LSM	lanthanum strontium manganate
OCV	open circuit voltage
RNL	Risø National Laboratory
RWGS	reversible water gas shift
ScSZ	scandium stabilized zirconium
SOEC	solid oxide electrolysis cell
TPB	triple phase boundary
YSZ	yttrium stabilized zirconium

### English letter

$a$	pre-exponential factor in sticking coefficient expression
$A$	pre-exponential factor of the Arrhenius form (in terms of cm, mol and s)
$b$	temperature exponent in sticking coefficient expression
$c$	concentration of species ( $\text{mol m}^{-3}$ )
$c_{(\text{Ni})}$	surface concentrations of the free surface active sites on the Ni surface ( $\text{mol m}^{-2}$ )
$c_{\text{O}(\text{Ni})}$	surface concentrations of O element on the Ni surface ( $\text{mol m}^{-2}$ )
$c_{\text{O}^{2-}(\text{YSZ})}$	the volumetric concentrations of interstitial oxygen in the YSZ ionic conductor ( $\text{mol m}^{-3}$ )
$c_{(\text{YSZ})}$	the volumetric concentrations of interstitial oxygen in the YSZ ionic conductor ( $\text{mol m}^{-3}$ )
$c_{\text{O}_2}^{\text{bulk}}$	the oxygen concentrations in the bulk ( $\text{mol m}^{-3}$ )
$c_{\text{O}_2}^{\text{TPB}}$	the oxygen concentrations at the TPB ( $\text{mol m}^{-2}$ )
$d$	activation energy in sticking coefficient expression ( $\text{J mol}^{-1}$ )
$D^{\text{eff}}$	effective diffusion coefficient ( $\text{m}^2 \text{s}^{-1}$ )
$D_{\text{Kn}}^{\text{eff}}$	effective Knudsen diffusion coefficient ( $\text{m}^2 \text{s}^{-1}$ )
$D_{\text{mole}}^{\text{eff}}$	effective molecular diffusion coefficient ( $\text{m}^2 \text{s}^{-1}$ )
$E$	activation energy ( $\text{kJ mol}^{-1}$ )
$F$	Faraday constant ( $96,384 \text{ C mol}^{-1}$ )
$i_0$	exchange current density ( $\text{A m}^{-2}$ )
$k$	reaction rate constant (in terms of m, mol and s)
$k_{\text{ec}}$	forward electrochemical reaction rate ( $\text{mol m}^{-2} \text{s}^{-1}$ )
$k_{-\text{ec}}$	reverse electrochemical reaction rate ( $\text{mol m}^{-2} \text{s}^{-1}$ )

$K_g$	number of gas species
$K_s$	number of surface species
$M$	molecular weight ( $\text{kg mol}^{-1}$ )
$n$	reaction order of the Arrhenius form
$n_t$	total number of electronic and ionic conductor particles
$n_{ep}$	fraction number of electronic conductor particles
$n_{ip}$	fraction number of ionic conductor particles
$N$	number of reactions
$p$	pressure (Pa)
$P_{ep}$	whole range connection probabilities of electronic conductor particles
$P_{ip}$	whole range connection probabilities of ionic conductor particles
$\bar{r}$	average pore radius (m)
$r_{ep}$	mean radius of the electronic conductor particle (m)
$R$	gas constant ( $8.314 \text{ mol}^{-1} \text{ K}^{-1}$ ) or source term of mass balance equation ( $\text{kg m}^{-3} \text{ s}^{-1}$ )
$\dot{s}$	net molar production rate of gaseous or surface species ( $\text{mol m}^{-2} \text{ s}^{-1}$ )
$S^0$	initial sticking coefficient
$S^{\text{eff}}$	effective reaction area per unit volume ( $\text{m}^2 \text{ m}^{-3}$ )
$S_{\text{Ni}}$	Ni active surface area per unit volume ( $\text{m}^2 \text{ m}^{-3}$ )
$S_{\text{TPB}}$	TPB active area per unit volume ( $\text{m}^2 \text{ m}^{-3}$ )
$T$	temperature (K)
$Q_{\text{elec,an}}$	electronic current source in anode ( $\text{A m}^{-3}$ )
$Q_{\text{elec,ca}}$	electronic current source in cathode ( $\text{A m}^{-3}$ )
$Q_{\text{ion,an}}$	ionic current source in anode ( $\text{A m}^{-3}$ )
$Q_{\text{ion,ca}}$	ionic current source in cathode ( $\text{A m}^{-3}$ )
$V$	diffusion volume
$V_{\text{elec,an}}$	electronic potential in anode (V)
$V_{\text{elec,ca}}$	electronic potential in cathode (V)
$V_{\text{ion,an}}$	ionic potential in anode (V)
$V_{\text{ion,ca}}$	ionic potential in cathode (V)
$V_{\text{ion,el}}$	ionic potential in electrolyte (V)
$V_{\text{ref,an}}$	reference potential in anode equal to OCV (V)
$V_{\text{ref,ca}}$	reference potential in cathode set to zero (V)
$W$	molecular weight of gas species ( $\text{kg mol}^{-1}$ )
$x$	molar fraction
$Z$	mean coordination number of electron and ionic conductor particles
$Z_{ep}$	coordination number of electron conductor particles
$Z_{ip}$	coordination number of ionic conductor particles

#### Greek letters

$\alpha$	charge transfer coefficient
$\beta$	cathode electrochemical kinetics parameter
$\gamma$	the sum of all of the surface reactants stoichiometric coefficients
$\Gamma$	surface sites density ( $\Omega^{-1} \text{ m}^{-2}$ )
$\varepsilon$	porosity or parameter modeling the species coverage
$\eta_{\text{an}}$	anode overpotential (V)
$\eta_{\text{ca}}$	cathode overpotential (V)
$\theta$	surface coverage or contact angle between the electronic and ionic conductors (rad)
$\mu$	parameter modeling the species coverage
$\nu'$	stoichiometric coefficient of the reactants
$\nu''$	stoichiometric coefficient of the products
$\sigma_{\text{elec,ca}}^{\text{eff}}$	corresponding electronic conductor phase effective conductivity in cathode ( $\text{S m}^{-1}$ )
$\sigma_{\text{ion,an}}^{\text{eff}}$	corresponding ionic conductor phase effective conductivity in anode ( $\text{S m}^{-1}$ )
$\sigma_{\text{ion,ca}}^{\text{eff}}$	corresponding ionic conductor phase effective conductivity in cathode ( $\text{S m}^{-1}$ )
$\sigma_{\text{ion,el}}^{\text{eff}}$	corresponding ionic conductor phase effective conductivity in electrolyte ( $\text{S m}^{-1}$ )

$\tau$	tortuosity
$\chi$	species symbol
$\partial\Omega$	computational domain

#### Subscripts

ac	anode chamber
act	active layer
an	anode
ca	cathode
cc	cathode chamber
ec	electrochemical reactions
el	electrolyte
elec	electronic
ep	electronic conductor particle
$i$	reactions index
$g$	gas-phase species
ion	ionic
ip	ionic conductor particle
Kn	Knudsen
mole	molecular
ref	reference
sp	support layer
t	total

#### Superscripts

0	parameter at equilibrium conditions
bulk	bulk phase
eff	effective
TPB	triple phase boundary

#### References

- [1] C. Graves, S.D. Ebbesen, M. Mogensen, K.S. Lackner, Renewable and Sustainable Energy Reviews 15 (2011) 1–23.
- [2] C.M. Stoots, J.E. O'Brien, J.S. Herring, J.J. Hartvigsen, Journal of Fuel Cell Science and Technology 6 (2009) 1–12.
- [3] C. Stoots, J. O'Brien, J. Hartvigsen, International Journal of Hydrogen Energy 34 (2009) 4208–4215.
- [4] C. Graves, S.D. Ebbesen, M. Mogensen, Solid State Ionics 192 (2011) 398–403.
- [5] Z. Zhan, W. Kobsiriphat, J.R. Wilson, M. Pillai, I. Kim, S.A. Barnett, Energy Fuel 23 (2009) 3089–3096.
- [6] P. Kim-Lohsoontorn, J. Bae, Journal of Power Sources 196 (2011) 7161–7168.
- [7] Q. Fu, C. Mabilat, M. Zahid, A. Brisse, L. Gautier, Energy & Environmental Science 3 (2010) 1382–1397.
- [8] J.E. O'Brien, M.G. McKellar, E.A. Harvego, C.M. Stoots, International Journal of Hydrogen Energy 35 (2010) 4808–4819.
- [9] W.L. Becker, R.J. Braun, M. Penev, M. Melaina, Energy 47 (2012) 99–115.
- [10] S.D. Ebbesen, J. Høgh, K.A. Nielsen, J.U. Nielsen, M. Mogensen, International Journal of Hydrogen Energy 36 (2011) 7363–7373.
- [11] C.M. Stoots, J.E. O'Brien, K.G. Condie, J.J. Hartvigsen, International Journal of Hydrogen Energy 35 (2010) 4861–4870.
- [12] W. Li, H. Wang, Y. Shi, N. Cai, International Journal of Hydrogen Energy in press.
- [13] S.D. Ebbesen, C. Graves, M. Mogensen, International Journal of Green Energy 6 (2009) 646–660.
- [14] M. Ni, M.K.H. Leung, D.Y.C. Leung, Journal of Power Sources 163 (2006) 460–466.
- [15] D. Grondin, J. Deseure, P. Ozil, J.P. Chabriot, B. Grondin-Perez, A. Brisse, Journal of Power Sources 196 (2011) 9561–9567.
- [16] J. Laurencin, D. Kane, G. Delette, J. Deseure, F. Lefebvre-Joud, Journal of Power Sources 196 (2011) 2080–2093.
- [17] J. Udagawa, P. Aguiar, N.P. Brandon, Journal of Power Sources 180 (2008) 46–55.
- [18] S.H. Chan, X.J. Chen, K.A. Khor, Journal of Power Sources 111 (2002) 320–328.
- [19] M. Ni, Chemical Engineering Journal 164 (2010) 246–254.
- [20] Y. Shi, Y. Luo, N. Cai, J. Qian, S. Wang, W. Li, H. Wang, Electrochimica Acta 88 (2013) 644–653.
- [21] M. Ni, Journal of Power Sources 202 (2012) 209–216.
- [22] M. Ni, International Journal of Hydrogen Energy 37 (2012) 6389–6399.
- [23] E.S. Hecht, G.K. Gupta, H. Zhu, A.M. Dean, R.J. Kee, L. Maier, O. Deutschmann, Applied Catalysis A: General 295 (2005) 40–51.
- [24] H.Y. Zhu, R.J. Kee, Journal of Electrochemical Society 153 (2006) A1765–A1772.
- [25] W.G. Bessler, S. Gewies, M. Vogler, Electrochimica Acta 53 (2007) 1782–1800.
- [26] G.M. Goldin, H. Zhu, R.J. Kee, D. Bierschenk, S.A. Barnett, Journal of Power Sources 187 (2009) 123–135.

- [27] V.M. Janardhanan, O. Deutschmann, *Journal of Power Sources* 162 (2006) 1192–1202.
- [28] A. Bieberle, L.J. Gauckler, *Solid State Ionics* 146 (2002) 23–41.
- [29] Y. Shi, N. Cai, C. Li, C. Bao, E. Croiset, J. Qian, Q. Hu, S. Wang, *ECS Transactions* 7 (2007) 1889–1899.
- [30] Y. Shi, N. Cai, C. Li, C. Bao, E. Croiset, J. Qian, Q. Hu, S. Wang, *Journal of Power Sources* 172 (2007) 235–245.
- [31] Y. Shi, N. Cai, C. Li, C. Bao, E. Croiset, J. Qian, Q. Hu, S. Wang, *Journal of Power Sources* 172 (2007) 246–252.
- [32] Y. Shi, N. Cai, C. Li, C. Bao, E. Croiset, J. Qian, Q. Hu, S. Wang, *Journal of Electrochemical Society* 155 (2008) B270–B280.
- [33] C. Li, Y. Shi, N. Cai, *Journal of Power Sources* 195 (2010) 2266–2282.
- [34] P. Costamagna, P. Costa, V. Antonucci, *Electrochimica Acta* 43 (1998) 375–394.
- [35] S.H. Chan, Z.T. Xia, *Journal of Electrochemical Society* 148 (2001) A388–A394.
- [36] E.A. Mason, A.P. Malinauskas, *Gas Transport in Porous Media: The Dusty-gas Model*, Elsevier, New York, 1983.
- [37] B. Todd, J.B. Young, *Journal of Power Sources* 110 (2002) 186–200.
- [38] R.J. Kee, M.E. Coltrin, P. Blarborg, *Chemically Reacting Flow*, John Wiley & Sons, Inc., Hoboken, NJ, 2003.
- [39] J. Divisek, R. Wilkenh O Ner, Y. Volfkovich, *Journal of Applied Electrochemistry* 29 (1999) 153–163.